

Dynamic *Arabidopsis* P5CS filament facilitates substrate channelling

Received: 8 September 2023

Accepted: 11 April 2024

Published online: 13 May 2024

Check for updates

Chen-Jun Guo^{1,4}, Tianyi Zhang^{1,4}, Qingqing Leng¹, Xian Zhou¹, Jiale Zhong¹ & Ji-Long Liu^{1,2,3}✉

In plants, the rapid accumulation of proline is a common response to combat abiotic stress^{1–7}. Delta-1-pyrroline-5-carboxylate synthase (P5CS) is a rate-limiting enzyme in proline synthesis, catalysing the initial two-step conversion from glutamate to proline⁸. Here we determine the first structure of plant P5CS. Our results show that *Arabidopsis thaliana* P5CS1 (AtP5CS1) and P5CS2 (AtP5CS2) can form enzymatic filaments in a substrate-sensitive manner. The destruction of AtP5CS filaments by mutagenesis leads to a significant reduction in enzymatic activity. Furthermore, separate activity tests on two domains reveal that filament-based substrate channelling is essential for maintaining the high catalytic efficiency of AtP5CS. Our study demonstrates the unique mechanism for the efficient catalysis of AtP5CS, shedding light on the intricate mechanisms underlying plant proline metabolism and stress response.

Delta-1-pyrroline-5-carboxylate synthase (P5CS) is a key enzyme in proline biosynthesis pathway. This enzyme catalyses a two-step reaction that converts glutamate to L-glutamate-5-phosphate (G5P) and then to L-glutamate-5-semialdehyde. L-Glutamate-5-semialdehyde will spontaneously cyclize and reach equilibrium with delta-1-pyrroline-5-carboxylate (P5C) (Extended Data Fig. 1a). The final product P5C is an essential precursor for proline biosynthesis⁸. As a bifunctional enzyme, P5CS has two structural domains: the glutamate kinase (GK) domain and the glutamyl phosphate reductase (GPR) domain. In prokaryotes, GK and GPR are separate enzymes, and in most eukaryotes they are fused into a bifunctional P5CS⁹ (Extended Data Fig. 1b,c and Supplementary Fig. 1). We have found that *Drosophila melanogaster* P5CS (DmP5CS) can form cytoophidium, and purified DmP5CS can also form metabolic filaments *in vitro*¹⁰. It is uncertain whether filamentation of P5CS is a conserved phenomenon or a special case of a few species. Except for DmP5CS, the full-length structure of P5CS has not been reported.

In this Letter, we choose AtP5CS as the model to investigate the structure and function of plant P5CS. The two P5CSs in *Arabidopsis thaliana*, AtP5CS1 and AtP5CS2, share 89% identity in protein sequence. AtP5CS2 is easily expressed in *Escherichia coli* with Small Ubiquitin-like Modifier (SUMO)-tag. During purification, AtP5CS2 showed a wide

range of molecular weights in size exclusion chromatography (Supplementary Fig. 2). The oligomerization state of AtP5CS2 was checked with negative-staining electron microscopy (EM). At APO state (ligand-free state) (with 20 mM Tris-HCl, 150 mM NaCl, 10 mM MgCl₂, pH = 8.0), no filament was observed (Extended Data Fig. 3a). At P5CS2, filaments will appear once there is adenosine triphosphate (ATP) or glutamate in the buffer (Fig. 1a). When both ATP and glutamate are present, longer filaments were observed (Fig. 1b). The average length of AtP5CS2 filaments increased significantly when all substrates are added (mixed state) compared with all other conditions (Fig. 1b).

After numerous attempts, we were unable to obtain a stable, active AtP5CS1 protein through the SUMO-tag expression system. Consequently, we explored direct expression using the N-terminal 6His system and successfully acquired active AtP5CS1 protein (Supplementary Fig. 3). However, application of size exclusion chromatography led to the inactivation of AtP5CS1, and we only used one-step affinity purification for AtP5CS1. To avoid the affection of glycerol on the following cryo-EM study, we opted for a low-salt buffer without glycerol for protein elution.

Upon examination through negative-staining EM, we discovered the filamentation of AtP5CS1 showed a pattern similar to that of AtP5CS2 (Fig. 1a,c and Extended Data Fig. 3). Interestingly, under

¹School of Life Science and Technology, ShanghaiTech University, Shanghai, China. ²Department of Physiology, Anatomy and Genetics, University of Oxford, Oxford, UK. ³Shanghai Clinical Research and Trial Center, Shanghai, China. ⁴These authors contributed equally: Chen-Jun Guo, Tianyi Zhang.

✉e-mail: liujl3@shanghaitech.edu.cn

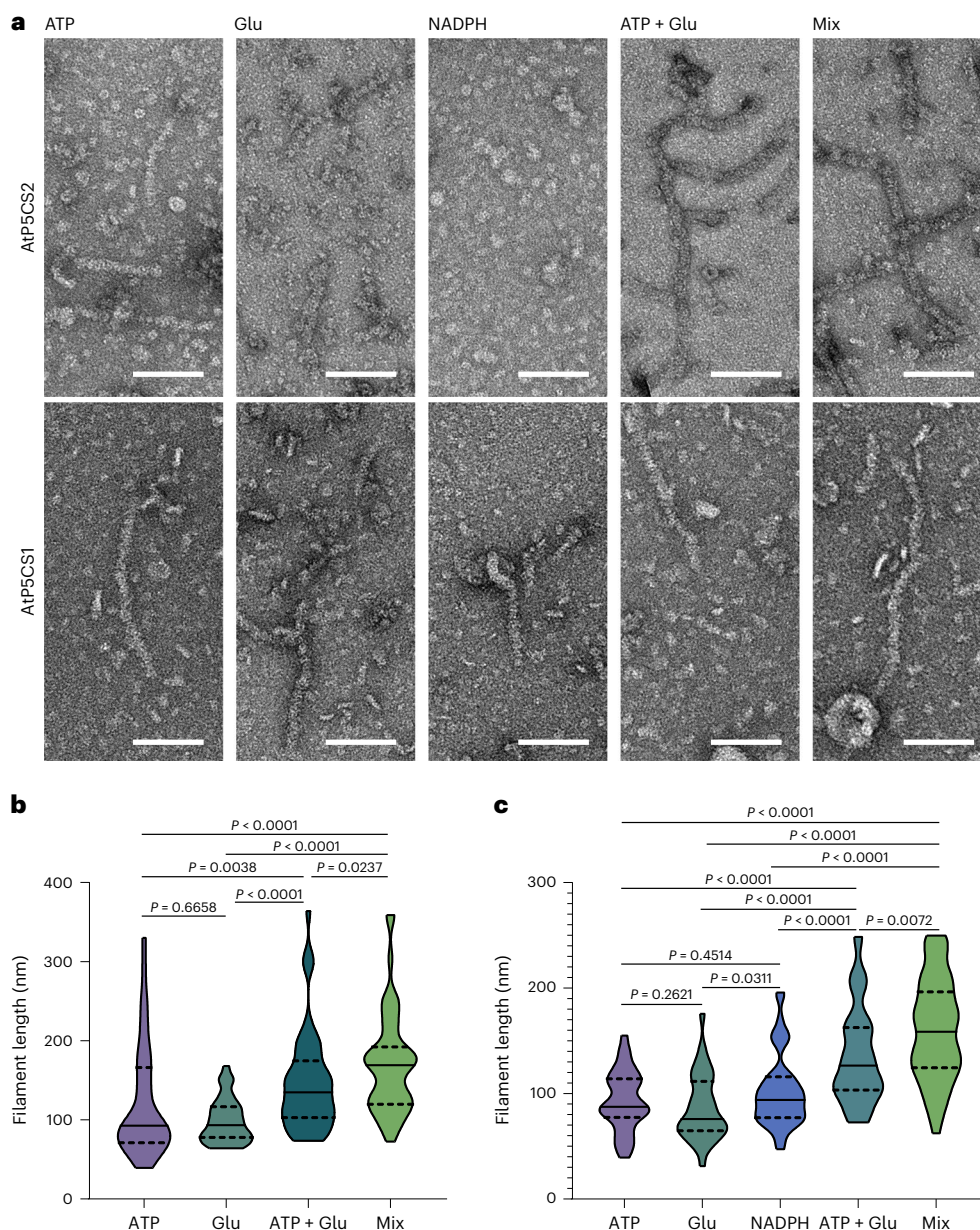


Fig. 1 | Both AtP5CS1 and AtP5CS2 form active filaments in vitro and respond to the ligands. a, Negative-staining EM micrographs of AtP5CS2 and AtP5CS1 incubated with different substrate combinations. Scale bars, 100 nm. **b**, Statistical analysis of AtP5CS2 filament length under different substrate conditions. Truncated violin plots show the medians (solid lines) and quartiles

(dashed lines). Two-sided Mann–Whitney test was used. **c**, Statistical analysis of AtP5CS1 filament length under different substrate conditions. Truncated violin plots show the medians (solid lines) and quartiles (dashed lines). Two-sided Mann–Whitney test was used.

conditions with only reduced nicotinamide adenine dinucleotide phosphate (NADPH) present, the AtP5CS1 sample showed a capacity for filament formation, while AtP5CS2 maintained its oligomeric state. With these negative staining and statistical data, we conclude both AtP5CS1 and AtP5CS2 could form filaments, and this filamentation is regulated by their substrates. Compared with DmP5CS, the regulation of AtP5CS filament is different. For DmP5CS, the contribution of glutamate is greater than that of ATP¹¹. For AtP5CS1 and AtP5CS2, both glutamate and ATP promote filament formation at similar degrees (Fig. 1b,c). Both DmP5CS and AtP5CS form the longest filaments at mixed state.

We first determined the cryo-EM structure of mixed-state AtP5CS2 (Extended Data Fig. 4 and Supplementary Table 1). Using single-particle analysis and focus refinement strategy, we obtained a map containing about five helical units of AtP5CS2 (Fig. 2a). Each helical unit is a

tetramer, in which the GK domain is located at the core as one tetramer and the GPR domain is located on both sides as two dimers. Helical units are arranged in a perpendicular way, and an obvious interface consists of hooks located on the helical axis. Interestingly, in our map, there is no apparent interaction between adjacent GPRs, which is thought to be important for the activity of DmP5CS.

The only connection between the GK domain and the GPR domain is a flexible linker, and large motion is observed between the GK tetramer and the GPR dimer. In the overall reconstruction, only a blob can be seen at the GPR domain. After focus refinement, the central GK tetramer could reach an average 3.3 Å resolution (Extended Data Fig. 4), but no high-resolution reconstruction for the GPR domain was made. By fitting the full-length model generated by AlphaFold2 into our map and with manual adjustments, we built the model for AtP5CS2 filament (Fig. 2b). The hook between adjacent helical units

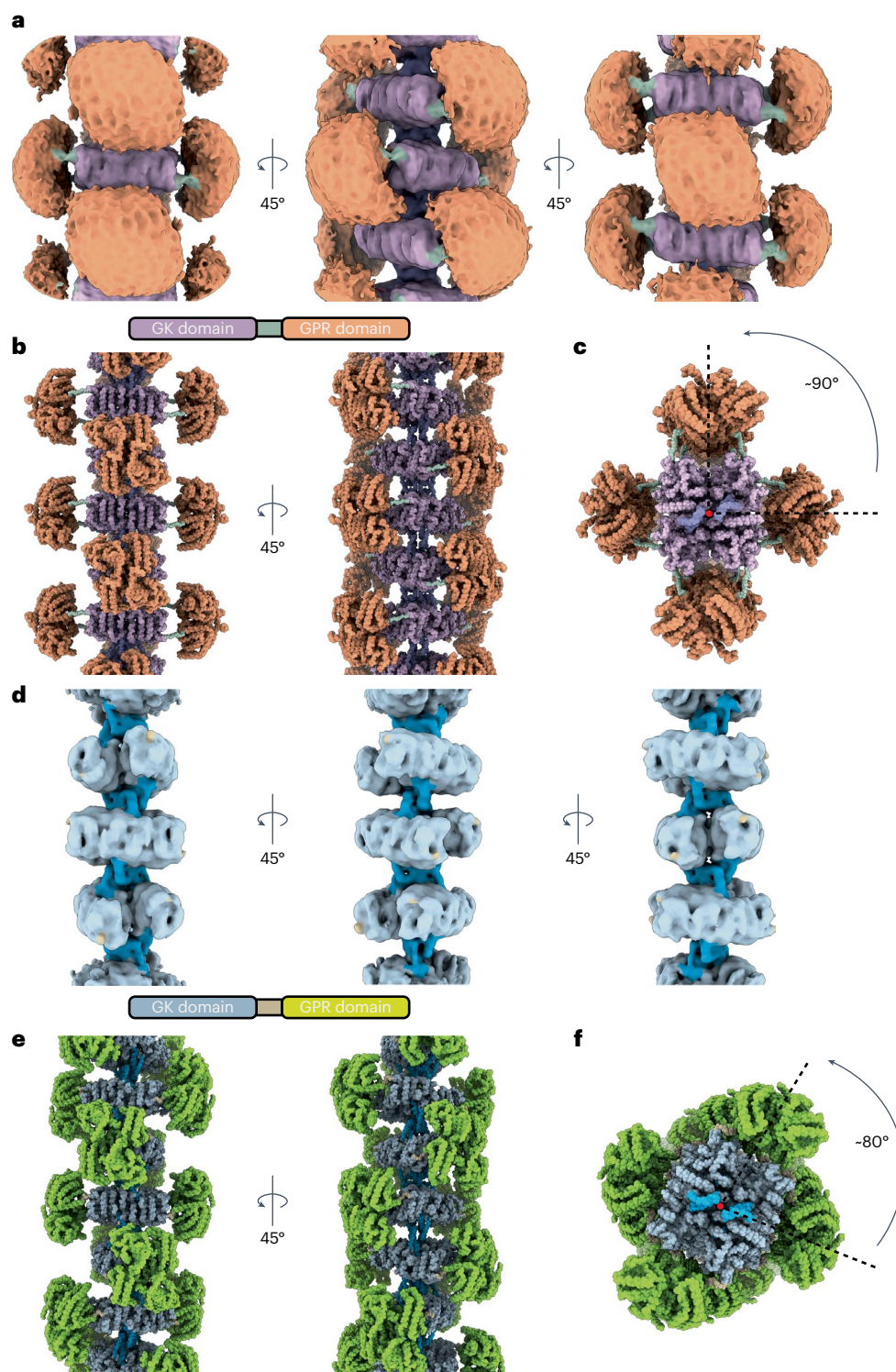


Fig. 2 | Overall structure of AtP5CS filaments. a, Density map of AtP5CS2 filament. GK domain, hook, GPR domain and linker of AtP5CS2 filament are coloured differently. **b**, Proposed model for the AtP5CS2 filament. This model was generated by using the predicted full-length model of AtP5CS2 from AlphaFold2 and fitting it into our density map. **c**, The top view of the AtP5CS2

filament. **d**, Density map of AtP5CS1 filament. GK domain, hook, GPR domain and linker of AtP5CS1 filament are coloured differently. **e**, Proposed model for the AtP5CS1 filament. This model was generated by using the predicted full-length model of AtP5CS1 from AlphaFold2 and fitting it into our density map. **f**, The top view of the AtP5CS1 filament.

can be seen clearly in the side view of this model, and the whole filament appears as a cross in the top view due to the orthogonal assembly of AtP5CS2 (Fig. 2c).

After obtaining active protein, we prepared cryo-samples of mixed-state AtP5CS1. A map containing approximately five helical

units was obtained (Fig. 2d, Extended Data Fig. 5 and Supplementary Table 1). Similar to the AtP5CS2 filament, the AtP5CS1 filament is composed of tetramers serving as the basic helical unit. Adjacent helical units interact through assembly interfaces comprising hooks. Differing from the AtP5CS2 filament, the adjacent helical units in the AtP5CS1

conserved functional amino acids K20, D177 and K242 of the kinase family. Besides, between the RGP and ADP, there is a magnesium ion that was previously observed in the model of DmP5CS. The conserved position for magnesium implies its potential function during the catalysis of GK.

In the model of AtP5CS1, the substrate ATP has been captured (Extended Data Fig. 7c). Similar to the ADP binding in AtP5CS2, the adenine group is stabilized by the ATP binding loop of AtP5CS1, and the triphosphate group interacts with the conserved functional amino acids K20, D177 and K242 (Extended Data Fig. 7d). We identified a small density located near the RGP binding amino acids S60, A62 and D157, implying that this could be the density of the substrate glutamate. However, due to resolution limitations, we did not model this density. When aligning the two structures, the amino acids participating in ligand recognition are conserved, and the overall conformation is similar with a root-mean-squared deviation of 0.6 Å (Extended Data Fig. 7e). The mutant variant F129A in Vigna shows the ability to eliminate the feedback inhibition of P5CS. In our model, the corresponding F128 is positioned near the centre of the AtP5CS tetramer. However, it is distanced from the catalytic pocket (Supplementary Fig. 5). The mechanism by which F128A eliminates feedback inhibition requires further experiments for a comprehensive explanation.

The DmP5CS filament forms in a double helix pattern through the interaction of hooks and adjacent GPRs. However, the GPR domain of AtP5CS was found to be highly flexible based on two- and three-dimensional (2D and 3D) classification results. The representative classes of 2D classification show that the GK domain in the centre of both AtP5CS1 and AtP5CS2 remains in high resolution with clear details. A clear but small signal is resolved for the connection by the hook of adjacent helical units for both AtP5CS1 and AtP5CS2. In AtP5CS2, the GPR on the side appears in a blurred and light grey manner, while in AtP5CS1, the GPR is even more blurred and exhibits a lighter colour (Fig. 3a). These 2D classification results indicate the stable interface of AtP5CS filaments is located on the GK domain.

We tried to capture potential transient stable GPR locations of AtP5CS2 by 3D classification. After the particles were re-centred from the GK tetramer to the hook, the quality of 3D classification results was improved and the density of GPR dimers became solid in many classes (Extended Data Fig. 8). None of these solid GPR dimers stays at the central line of AtP5CS2 tetramer; that is, the linkers between GK and GPR are not perpendicular to the helical axis. Comparing the locations of GPR dimers in different classes, we found the GPR dimer can rotate around the GK tetramer in a considerably wide range (Extended Data Fig. 9a–d). Some transient interactions become possible during the rotation. In class II, the most possible interaction is between GPR dimer and a GK tetramer from an adjacent helical unit. The GK tetramer model and GPR dimer model were fitted into the map. A plausible interaction between E347 and K131/135 will be seen with proper rotamers (Extended Data Fig. 9e,f). We also evaluated potential interactions between two GPR dimers. In class II, two GPR dimers from adjacent AtP5CS2 tetramers swing toward each other (Extended Data Fig. 9g). Two pairs of Asn and Gln were found at the tip of the GPR dimer. In the fitted models, the distances between side

chains of N586 pair and Q557 pair are more than 10 Å (Extended Data Fig. 9h), which is too far for direct interactions.

The sequence of the hook is conserved between AtP5CS1 and AtP5CS2 (Fig. 3b). The stable interface of both the AtP5CS1 and AtP5CS2 filaments is composed of four hooks from two adjacent helical units. Focusing on one side of the helical interface, four pairs of hydrogen bonds (V76–A81', S78–F80', F80–S78' and A81–V76') form between the backbones of a pair of hooks from adjacent helical units. This interaction provides a direct connection between adjacent helical units and is conserved in the previously determined DmP5CS structures (Fig. 3c).

In the helical interface of both AtP5CS1 and AtP5CS2, the pi–pi interaction of F80 with another F80 from the same helical unit forms a bridge-like structure. Due to the symmetry, the other two protomers from adjacent helical units also form the same structure but in an inverted orientation. Together, the two bridges combine to form a lock structure that connects and stabilizes adjacent helical units along the helical axis (Fig. 3d).

Comparing the AtP5CS and DmP5CS structures, the key residue F80 in AtP5CS has been replaced by methionine (Fig. 3b,d). There is a distinct difference in the formation of the lock structure, as the four methionines gather together and interact with each other, unlike the two bridges of a lock structure in AtP5CS that maintain distance from one another. In DmP5CS, the side chain of R124 forms an electrostatic interaction with the side chain of E116, thereby stabilizing the lock structure. However, in AtP5CS, the amino acid corresponding to R124 is replaced by the conserved alanine, and this electrostatic interaction no longer exists. This change may make the maintenance of the lock structure more reliant on the pi–pi interactions between F80s.

Multiple sequence alignment (MSA) reveals that the hook is present in both plants and animals but has many differences. Compared to animal P5CS, the following loop length of plant P5CS is noticeably shorter, and the amino acids in the relative position of F80 in plants are mainly phenylalanine, while in animals they are mainly methionine or valine (Fig. 3b). The overall conformation of the hook structure is a helix–loop–helix and exhibits a similar angle in both DmP5CS and AtP5CS. However, when aligning the long helix of the hook from AtP5CS1 and AtP5CS2 to DmP5CS, the short helix of the hook shows a rotation around the long helix of approximately 44° and 42°, respectively (Fig. 3e,f). This results in different positions of M123 and F80, and the change in the angle of the hook provides a structural basis for the difference in helical twist between DmP5CS and AtP5CSs. In DmP5CS, the contact loop of the GPR domain is necessary for filament formation. Mutation of key residues in the DmP5CS contact loop will abolish filament formation. But in AtP5CS, whether the GPR domain is necessary for filament formation is not clear. Considering the conservation in the filament interface and the potential benefits in terms of expression and purification, along with the absence of an artificial His tag in the N-terminal, we expressed and purified truncated AtP5CS2 protein consisting of residues 1–290 (referred to as AtP5CS2-GK) to explore this question.

Similar to full-length AtP5CS2, AtP5CS2-GK formed filaments quickly after being incubated with substrates (Fig. 4a). Few filaments were observed for APO AtP5CS2-GK (Fig. 4a). After being incubated with

Fig. 4 | Connecting filamentation and function of AtP5CS. **a**, Negative-staining EM micrographs of AtP5CS2 GK domain incubated with different substrates. Regions in red rectangles are zoomed in on the right of the original micrographs. Scale bars, 200 nm for original micrographs and 50 nm for zoomed-in micrographs. **b**, Statistical analysis of AtP5CS2 filament length under different conditions. Violin plots show the medians (solid lines) and quartiles (dashed lines). Two-sided Mann–Whitney test was used. **c**, Negative-staining results of AtP5CS2-WT and AtP5CS2-F80A. Scale bars, 100 nm. **d**, GPR activity of AtP5CS2-WT and AtP5CS2-F80A, measured by the change of absorbance at 340 nm (A340). Error bars show the upper and lower bounds of data ($n = 3$ technical repeats). **e**, GK activity of AtP5CS2-WT and AtP5CS2-F80A, measured by phosphate

generation. Error bars show the upper and lower bounds of data ($n = 3$ technical repeats). **f**, Model of AtP5CS2 filament dynamics. The blue rounded rectangles represent GK tetramers, and the orange sticks represent hooks. Two different states of hooks are shown in this figure: the open one (APO and products released states) and the locked one (substrates binding and catalysing states). **g**, Possible mechanisms of how a filament contributes to substrates channelling. Three GK tetramers (grey) and one GPR dimer (light pink or light blue) are shown here. GPR dimer can rotate up and down around the central GK tetramer, and one farthest position of GPR dimer is shown here. The activity centre of AtP5CS2 GPR is inferred from DmP5CS model (PDB: 7WXI), the key amino acid C543 for catalysing is shown. The red arrows show two possible G5P transfer paths.

We use site mutagenesis to study the function of AtP5CS2 filament. AtP5CS2-F80A mutant was constructed according to structural analysis. At APO state, no filament was observed for both WT and F80A AtP5CS2 (Fig. 4c). But after being incubated with all substrates, WT and mutant AtP5CS2 showed conspicuous difference (Fig. 4c). F80A mutation blocked the filament formation of AtP5CS2. We measured the overall activity of WT and F80A AtP5CS2 by decrease of absorbance at 340 nm (Fig. 4d). The decrease of absorbance at 340 nm showed good linearity within 10 min. The maximum reaction velocity (V_{\max}) of F80A mutant is 7.07 μmol of NADPH per min per μmol , only 30% of that of WT, which is 23.28 μmol of NADPH per min per μmol (Supplementary Table 2).

We tried to find how F80A mutation affected the overall activity of AtP5CS2. It has been assumed that P5CS could transfer the intermediate G5P between two domains because G5P is labile¹². Filamentation of P5CS may facilitate the channelling of G5P. To test this hypothesis, we measured the specific activity of GK domain in WT and F80A AtP5CS2 by phosphate assay (Fig. 4e). The activity of AtP5CS2-F80A GK domain is 364.27 μmol of Pi per min per μmol , which is slightly slower than that of the WT GK domain (396.24 μmol of Pi per min per μmol). The results show that G5P generation rates are much higher than NADPH consumption rates in both WT and F80A enzymes, which is consistent with human P5CS¹³. Despite the similar specific activity of GK domain, the G5P utilization efficiency in WT enzyme (5.9%) is much higher than in the F80A enzyme (1.9%) (Supplementary Table 2). Taken together, the F80A mutation impairs the activity of AtP5CS2 by reducing the efficiency of G5P channelling.

Recently, the filament structures and regulatory mechanisms of various enzymes have been revealed^{11,14–20}. In this study, we successfully expressed and purified active AtP5CS1 and AtP5CS2 proteins. By integrating the dynamic filament structures with enzyme functional assays, we propose a comprehensive model that sheds light on the intricate interplay between the catalytic and filamentation processes of AtP5CS2.

On one hand, the catalysing of AtP5CS2 serves as a driving force for filament formation. Our analyses, including negative-staining microscopy and statistical assessments, reveal that the longest filament forms during active catalysis, contrasting with the absence of filaments in the APO state. We propose a filamentation model wherein, in the APO state, specific residues surrounding the hook attract AtP5CS2 tetramers, and upon substrate binding or catalysis, these tetramers surmount the energy barrier, initializing the formation of stable filaments. The iterative interplay of attraction and catalysis processes contributes to the elongation of the AtP5CS2 filament (Fig. 4f).

On the other hand, the filamentation of AtP5CS2 plays a crucial role in enhancing the substrate channelling of G5P, facilitating the catalysis. The connection between the GK domain and GPR domain exhibits remarkable flexibility within the AtP5CS2 filament. Our 3D classification results indicate that the GPR dimer can undergo significant rotations around the GK tetramer. In certain classes of our model, compared to the ideally 'central position', the distance between the activity centres of GK and GPR is notably reduced (Extended Data Fig. 10). This reduction in the distance between the activity centres holds promising implications for efficient substrate channelling. Meanwhile, the distance between the GPR active site and the active site of GK from the neighbouring helical unit or the same helical unit is nearly identical, providing another potential approach for substrate transfer (Extended Data Fig. 10). The AtP5CS2 filament provides a unique platform for the rotational movement of the GPR dimer, facilitating substrate channelling (Fig. 4g).

Given the crucial role of AtP5CS1 in abiotic stress responses, the filament formation could positively impact the proline accumulation and stress responses in plants. Although AtP5CS2 filament enhances the channelling of G5P, only 5.9% G5P is used for P5C synthesis according to our enzyme activity assay (Supplementary Table 2). While the impact of AtP5CS filamentation in vivo requires further exploration,

enhancing the substrate channelling efficiency of P5CS may offer a new approach for stress-resistant crop breeding.

Methods

Molecular cloning and site-directed mutagenesis

A. thaliana complementary DNA is a kind gift from B. Zheng (Fudan University). AtP5CS1 and AtP5CS2 genes were cloned into *E. coli* expression vectors using one-step cloning method (ClonExpress II One Step Cloning Kit, Vazyme #C112). The primers used for molecular cloning are provided in Supplementary Table 1. The coding sequence of AtP5CS1 gene was cloned into pET28a vector, which resulted in a His₆-AtP5CS1 gene structure. The coding sequence of AtP5CS2 gene was cloned into a modified pET28a vector, where a SUMO-tag was fused at the N terminus of AtP5CS2, which resulted in a His₆-SUMO-AtP5CS2 gene structure.

Site-directed mutagenesis was also performed with one-step cloning method (ClonExpress II One Step Cloning Kit, Vazyme #C112). The primers used for mutagenesis are provided in Supplementary Table 3. All plasmids generated in this study had been sequenced to guarantee correct reconstruction.

AtP5CS1 protein expression and purification

The expression vector of AtP5CS1 was transformed into *E. coli* strain Rosetta (DE3). For protein expression, cells were first cultured at 37 °C to OD₆₀₀ = 0.8–1.0, then protein expression was induced with 40 μM isopropylthiogalactoside at 16 °C overnight. Cells were collected by centrifugation at 4 °C and 4,000 *g*, resuspended with lysis buffer (50 mM Tris-HCl at pH 8.0, 500 mM NaCl, 10% glycerol, 20 mM imidazole, 1 mM phenylmethylsulfonyl fluoride, 5 mM β -mercaptoethanol, 5 mM benzamidine, 2 $\mu\text{g ml}^{-1}$ leupeptin, and 2 $\mu\text{g ml}^{-1}$ pepstatin). Then the cell suspension was homogenized with ultrasonic homogenizer (Scientz-IID) or high-pressure homogenizer (Union-Biotech LH-03). The lysate was centrifuged at 4 °C, 18,000 *g* for 45 min. Supernatant from 1 l *E. coli* medium was incubated with 1 ml Ni-NTA agarose resin (QIAGEN) for 1 h. Then the resin was washed with 10 ml wash buffer containing 40 mM imidazole (with other components the same as lysis buffer). Then proteins were eluted with 2 ml elution buffer (25 mM Tris-HCl at pH 8.0, 150 mM NaCl, 250 mM imidazole, 5 mM β -mercaptoethanol). The elution was dispensed, snap-frozen with liquid nitrogen and stored at -80 °C before use.

AtP5CS2 protein purification

The expression vector of AtP5CS2 was transformed into *E. coli* strain Rosetta (DE3). For protein expression, cells were first cultured at 37 °C to OD₆₀₀ = 0.8–1.0, then protein expression was induced with 40 μM isopropylthiogalactoside at 16 °C overnight. Cells were collected by centrifugation at 4 °C and 4,000 *g*, resuspended with lysis buffer (50 mM Tris-HCl at pH 8.0, 500 mM NaCl, 10% glycerol, 20 mM imidazole, 1 mM phenylmethylsulfonyl fluoride, 5 mM β -mercaptoethanol, 5 mM benzamidine, 2 $\mu\text{g ml}^{-1}$ leupeptin and 2 $\mu\text{g ml}^{-1}$ pepstatin). Then the cell suspension was homogenized with ultrasonic homogenizer (Scientz-IID) or high-pressure homogenizer (Union-Biotech LH-03). The lysate was centrifuged at 4 °C, 18,000 *g* for 45 min. Supernatant from 1 l *E. coli* medium was incubated with 1 ml Ni-NTA agarose resin (QIAGEN) for 1 h. Then the resin was washed with 8 ml wash buffer containing 40 mM imidazole (with other components the same as lysis buffer). Then proteins were eluted with 2–4 ml elution buffer (50 mM Tris-HCl at pH 8.0, 500 mM NaCl, 250 mM imidazole, 5 mM β -mercaptoethanol). Yeast ULP1 was used to remove SUMO-tag. About 5 ml of storage buffer (25 mM Tris-HCl at pH 8.0 and 150 mM NaCl) was added together with ULP1 for optimal ULP1 activity. After being incubated and concentrated at 4 °C, proteins were further purified through Superose 6 Increase 10/300 GL (Cytiva) in storage buffer (25 mM Tris-HCl at pH 8.0 and 150 mM NaCl). Peak fractions were collected, concentrated, dispensed, snap-frozen with liquid nitrogen and stored at -80 °C before use.

AtP5CS activity NADPH assay

The reaction buffer contained 25 mM Tris–HCl at pH 8.0, 150 mM NaCl, 20 mM monosodium glutamate, 10 mM MgCl₂, 5 mM ATP (Takara, sodium salt, at pH 7.0) and 0.5 mM NADPH (Roche, tetrasodium salt). Reaction was started by adding 150 nM atP5CS (wild-type or mutant). Concentration of atP5CS was determined by BCA kit (Beyotime) using BSA as reference. The reaction was monitored at 25 °C in an SpectraMax i3 plate reader (Molecular Devices). The concentration of NADPH was converted from absorbance at 340 nm with molar extinction coefficients = 6.22 l mol⁻¹ cm⁻¹. The path length was determined by PathCheck Sensor in SpectraMax i3 plate reader.

AtP5CS activity Pi assay

The reaction buffer is the same as in the NADPH assay. About 150 nM enzyme was added to start the reaction. The reaction system was incubated at 25 °C. Reaction was terminated at different times by adding ice-cold 4 M perchloric acid to a final concentration of 1 M. Then perchloric acid was neutralized and precipitated with 2 M ice-cold KOH (final molar ratio perchloric acid to KOH = 1:1). The reaction mixture was centrifuged at 4 °C, 13,000 g for 15 min. The supernatant was used to determine Pi concentration with Malachite Green Phosphate Detection Kit (Beyotime).

Negative staining

Proteins were incubated with different substrates at 25 °C before negative staining. All substrates used here had the same concentration as in the activity assay. Proteins were diluted to about 2–4 μM. After incubation, the protein samples were applied to plasma-cleaned carbon-coated EM grids (400 mesh, EMCN). The grids were then washed twice in double-distilled H₂O and stained with 1–2% uranyl formate. Negative-staining EM grids were imaged with a Talos L120C microscope (FEI).

Cryo-EM grid preparation and data collection

For cryo-EM, purified atP5CS was diluted to approximately 5 μM in reaction buffer. The AtP5CS1 sample was incubated in reaction buffer for about 30 min on ice before vitrification. The AtP5CS2 sample was incubated in reaction buffer for about 60 min on ice before vitrification. The sample was applied on H₂/O₂ plasma-cleaned ANTCryo holy support film (Au300-R1.2/1.3) and then was immediately blotted for 3.0 s. The application and blot were repeated twice. Then the grid was plunge-frozen in liquid ethane cooled by liquid nitrogen using Vitrobot (Thermo Fisher) at 8 °C with 100% humidity. Images were collected on Titan Krios G3 (FEI) equipped with a K3 Summit direct electron detector (Gatan), operating in counting super-resolution mode at 300 kV with a total dose of 60 e⁻ Å⁻², subdivided into 50 frames in 2.8 s exposure using SerialEM²¹. The images were recorded at a nominal magnification of ×22,500 and a calibrated pixel size of 1.06 Å, with defocus ranging from 0.8 to 2.5 μm.

Data processing

For AtP5CS2, the image processing and reconstruction were performed with RELION 3.3 (refs. 22,23). We used MotionCor2 (ref. 24) and CTFIND4 (ref. 25) via RELION GUI for pre-processing. Only micrographs with estimated resolution better than 5 Å were selected for further processing. We first used manual picking and 2D classification to generate 2D templates for atP5CS2 filament. Then AtP5CS2 particles were picked with these templates. Particles were cleaned with several rounds of 2D classifications and two rounds of 3D classifications with C1 symmetry and then D2 symmetry. Finally, 223,041 particles were used for 3D reconstruction with D2 symmetry, and a filament with three helical units was acquired. Due to the flexibility of AtP5CS2 filament, we performed an additional 3D refinement with a mask around GK tetramer to get better resolution. Then we used contrast transfer function (CTF) refinement²⁶ and Bayesian polishing²⁷ to further improve the resolution. For detailed analysis on heterogeneity of GK monomer, we first applied D2 symmetry expansion on refined particles (after

CTF refinement and Bayesian polishing). Then we performed local 3D auto-refine on GK tetramer with C1 symmetry. Local resolution estimation was performed using Relion's own algorithm, and locally filtered maps were used for model building. To visualize the GPR domain, we re-extracted particles with shift along the helical axis to re-centre particles on the hook. Then after one round of 3D classification, some transient locations of GPR dimers can be visualized.

For AtP5CS1, the image processing and reconstruction were performed with CryoSPARC v4.4.0 (ref. 28). We used patch motion correction and patch CTF estimation for pre-processing. Only micrographs with estimated resolution better than 5 Å were selected for further processing. We first used AtP5CS2 filament map to generate 2D templates. We used these templates for the first round of template picking. Particles were extracted and cleaned with several rounds of 2D classifications. The first reconstruction was made with homogeneous reconstruction using AtP5CS2 filament as reference. Then new templates were generated from the first reconstruction of AtP5CS1 and used for a second round of template picking. Particles were extracted and cleaned with multiple rounds of 2D classifications. Finally, 222,855 particles were kept for final reconstruction. We first performed homogeneous reconstruction and non-uniform reconstruction²⁹. CTF refinement and reference-based motion correction were performed to improve the resolution. Then we used local refinement (to enable non-uniform reconstruction) with mask on central GK tetramer. The focus-refined map was used for model building.

Model building

The initial model of atP5CS GK domain was acquired through AlphaFold2 (ref. 30) database (<https://alphafold.com/>). The initial model was fitted into maps using UCSF Chimera³¹. Models were iteratively refined using a combination of Coot³² and phenix.real_space_refine in Phenix^{33,34}. For GPR dimer, model was generated with AlphaFold2 Multimer³⁵ on our local server with full-length atP5CS dimer as input. To analyse possible interactions of AtP5CS2 GPR dimers, rotamers of some residues in the fitted models were adjusted in UCSF Chimera using Dunbrack 2010 (ref. 36) rotamer library. UCSF ChimeraX³⁷ was also used for visualization purpose.

Evolutional analysis of P5CS

All P5CS protein sequences were downloaded from UniProt database. All MSAs used MAFFT (v7.511) with method E-INS-i³⁸. For phylogenetic tree reconstruction, we downloaded all sequences that were annotated with enzyme commission number '2.7.2.11' (GK) or '2.7.2.11' and '1.2.1.41' (P5CS). Only reviewed GK sequences were used. The sequences were filtered with length to remove too short or too long sequences (with Excel) and re-mapped to UniRef50 reference sequences. After alignment, gaps were removed by trimAl (1.2rev59)³⁹. A phylogenetic tree was built using IQTREE (v2.2)⁴⁰, and a model was auto-selected⁴¹ (Q.pfam+I+I+R7 was chosen according to Bayesian information criterion). A phylogenetic tree was visualized using FigTree (1.4.4)⁴² and coloured with Adobe Illustrator 2023. ESPript 3 (ref. 43) was used for MSA visualization. Sequence logos were generated using WebLogo 3 (ref. 44).

Reporting summary

Further information on research design is available in the Nature Portfolio Reporting Summary linked to this article.

Data availability

The structure data accession codes are EMD-35901, EMD-38855, PDB-8JOF and PDB-8Y2H.

References

1. Szekely, G. et al. Duplicated P5CS genes of *Arabidopsis* play distinct roles in stress regulation and developmental control of proline biosynthesis. *Plant J.* **53**, 11–28 (2008).

2. Yoshiba, Y. et al. Correlation between the induction of a gene for delta 1-pyrroline-5-carboxylate synthetase and the accumulation of proline in *Arabidopsis thaliana* under osmotic stress. *Plant J.* **7**, 751–760 (1995).
3. Strizhov, N. et al. Differential expression of two P5CS genes controlling proline accumulation during salt-stress requires ABA and is regulated by ABA1, ABI1 and AXR2 in *Arabidopsis*. *Plant J.* **12**, 557–569 (1997).
4. Hur, J., Jung, K. H., Lee, C. H. & An, G. H. Stress-inducible OsP5CS2 gene is essential for salt and cold tolerance in rice. *Plant Sci.* **167**, 417–426 (2004).
5. Zhao, M.-G., Chen, L., Zhang, L.-L. & Zhang, W.-H. Nitric reductase-dependent nitric oxide production is involved in cold acclimation and freezing tolerance in *Arabidopsis*. *Plant Physiol.* **151**, 755–767 (2009).
6. Schat, H., Sharma, S. S. & Vooijs, R. Heavy metal-induced accumulation of free proline in a metal-tolerant and a nontolerant ecotype of *Silene vulgaris*. *Physiol. Plant.* **101**, 477–482 (1997).
7. Singh, V. et al. Proline improves copper tolerance in chickpea (*Cicer arietinum*). *Protoplasma* **245**, 173–181 (2010).
8. Phang, J. M. Proline metabolism in cell regulation and cancer biology: recent advances and hypotheses. *Antioxid. Redox Signal.* **30**, 635–649 (2019).
9. Fichman, Y. et al. Evolution of proline biosynthesis: enzymology, bioinformatics, genetics, and transcriptional regulation. *Biol. Rev.* **90**, 1065–1099 (2015).
10. Zhang, B. et al. The proline synthesis enzyme P5CS forms cytoophidia in *Drosophila*. *J. Genet. Genomics* **47**, 131–143 (2020).
11. Zhong, J. et al. Structural basis of dynamic P5CS filaments. *Elife* **11**, e76107 (2022).
12. Arentson, B. W., Sanyal, N. & Becker, D. F. Substrate channeling in proline metabolism. *Front. Biosci.* **17**, 375–388 (2012).
13. Panza, E. et al. ALDH18A1 gene mutations cause dominant spastic paraplegia SPG9: loss of function effect and plausibility of a dominant negative mechanism. *Brain* **139**, e3 (2016).
14. Zhou, X. et al. *Drosophila* CTP synthase can form distinct substrate- and product-bound filaments. *J. Genet. Genomics* **46**, 537–545 (2019).
15. Zhou, X. et al. Structural basis for ligand binding modes of CTP synthase. *Proc. Natl Acad. Sci. USA* **118**, e2026621118 (2021).
16. Hansen, J. M. et al. Cryo-EM structures of CTP synthase filaments reveal mechanism of pH-sensitive assembly during budding yeast starvation. *Elife* **10**, e73368 (2021).
17. Lynch, E. M. & Kollman, J. M. Coupled structural transitions enable highly cooperative regulation of human CTPS2 filaments. *Nat. Struct. Mol. Biol.* **27**, 42–48 (2020).
18. Hu, H. H. et al. Filamentation modulates allosteric regulation of PRPS. *Elife* <https://doi.org/10.7554/eLife.79552> (2022).
19. Lu, G. M. et al. Structural basis of human PRPS2 filaments. *Cell Biosci.* **13**, 100 (2023).
20. Guo, C. J., Wang, Z. X. & Liu, J. L. Structural basis for activation and filamentation of glutaminase. *Cell Res.* **34**, 76–79 (2024).
21. Mastronarde, D. N. Automated electron microscope tomography using robust prediction of specimen movements. *J. Struct. Biol.* **152**, 36–51 (2005).
22. Scheres, S. H. W. RELION: implementation of a Bayesian approach to cryo-EM structure determination. *J. Struct. Biol.* **180**, 519–530 (2012).
23. Zivanov, J. et al. New tools for automated high-resolution cryo-EM structure determination in RELION-3. *Elife* **7**, e42166 (2018).
24. Zheng, S. Q. et al. MotionCor2: anisotropic correction of beam-induced motion for improved cryo-electron microscopy. *Nat. Methods* **14**, 331–332 (2017).
25. Rohou, A. & Grigorieff, N. CTFIND4: fast and accurate defocus estimation from electron micrographs. *J. Struct. Biol.* **192**, 216–221 (2015).
26. Zivanov, J., Nakane, T. & Scheres, S. H. W. Estimation of high-order aberrations and anisotropic magnification from cryo-EM data sets in RELION-3.1. *IUCr J* **7**, 253–267 (2020).
27. Zivanov, J., Nakane, T. & Scheres, S. H. W. A Bayesian approach to beam-induced motion correction in cryo-EM single-particle analysis. *IUCr J* **6**, 5–17 (2019).
28. Punjani, A., Rubinstein, J. L., Fleet, D. J. & Brubaker, M. A. cryoSPARC: algorithms for rapid unsupervised cryo-EM structure determination. *Nat. Methods* **14**, 290–296 (2017).
29. Punjani, A., Zhang, H. & Fleet, D. J. Non-uniform refinement: adaptive regularization improves single-particle cryo-EM reconstruction. *Nat. Methods* **17**, 1214–1221 (2020).
30. Jumper, J. et al. Highly accurate protein structure prediction with AlphaFold. *Nature* **596**, 583–589 (2021).
31. Pettersen, E. F. et al. UCSF Chimera—a visualization system for exploratory research and analysis. *J. Comput. Chem.* **25**, 1605–1612 (2004).
32. Emsley, P., Lohkamp, B., Scott, W. G. & Cowtan, K. Features and development of Coot. *Acta Crystallogr. D* **66**, 486–501 (2010).
33. Adams, P. D. et al. PHENIX: a comprehensive Python-based system for macromolecular structure solution. *Acta Crystallogr. D* **66**, 213–221 (2010).
34. Afonine, P. V. et al. Real-space refinement in PHENIX for cryo-EM and crystallography. *Acta Crystallogr. D* **74**, 531–544 (2018).
35. Evans, R. et al. Protein complex prediction with AlphaFold-Multimer. Preprint at *bioRxiv* <https://doi.org/10.1101/2021.10.04.463034> (2022).
36. Shapovalov, M. V. & Dunbrack, R. L. Jr. A smoothed backbone-dependent rotamer library for proteins derived from adaptive kernel density estimates and regressions. *Structure* **19**, 844–858 (2011).
37. Goddard, T. D. et al. UCSF ChimeraX: meeting modern challenges in visualization and analysis. *Protein Sci.* **27**, 14–25 (2018).
38. Katoh, K., Kuma, K.-i, Toh, H. & Miyata, T. MAFFT version 5: improvement in accuracy of multiple sequence alignment. *Nucleic Acids Res.* **33**, 511–518 (2005).
39. Capella-Gutiérrez, S., Silla-Martínez, J. M. & Gabaldón, T. trimAl: a tool for automated alignment trimming in large-scale phylogenetic analyses. *Bioinformatics* **25**, 1972–1973 (2009).
40. Minh, B. Q. et al. IQ-TREE 2: new models and efficient methods for phylogenetic inference in the genomic era. *Mol. Biol. Evol.* **37**, 1530–1534 (2020).
41. Kalyaanamoorthy, S., Minh, B. Q., Wong, T. K. F., von Haeseler, A. & Jermini, L. S. ModelFinder: fast model selection for accurate phylogenetic estimates. *Nat. Methods* **14**, 587–589 (2017).
42. Rambaut, A. FigTree 1.4.4. *GitHub* <https://github.com/rambaut/figtree> (2018).
43. Robert, X. & Gouet, P. Deciphering key features in protein structures with the new ENDScript server. *Nucleic Acids Res.* **42**, W320–W324 (2014).
44. Crooks, G. E., Hon, G., Chandonia, J. M. & Brenner, S. E. WebLogo: a sequence logo generator. *Genome Res.* **14**, 1188–1190 (2004).

Acknowledgements

We thank B. Zheng for providing the cDNA of *A. thaliana*. EM data were collected at the ShanghaiTech Cryo-EM Imaging Facility. We thank the Molecular and Cell Biology Core Facility at the School of Life Science and Technology, ShanghaiTech University, and Shanghai Frontiers Science Center for Biomacromolecules and Precision Medicine for providing technical support. This work was supported by grants to J.-L.L. from the Ministry of Science and Technology of China (number 2021YFA0804700), National Natural Science Foundation of China (number 31771490), Shanghai Science and Technology Commission (number 20JC1410500),

UK Medical Research Council (grant numbers MC_UU_12021/3 and MC_U137788471).

Author contributions

C.-J.G. initiated the project and cloned and established the expression system for target genes. T.Z. performed the functional assays, phylogenetic analysis, cryo-EM data processing, model building and structure refinement. C.-J.G. and T.Z. expressed and purified the proteins, prepared samples for EM studies, collected cryo-EM data, analysed experiments, visualized results and wrote the paper. Q.L., X.Z. and J.Z. assisted in the protein purification, functional assays or data analysis. J.-L.L. revised the paper, obtained the funding and supervised the project.

Competing interests

The authors declare no competing interests.

Additional information

Extended data is available for this paper at <https://doi.org/10.1038/s41477-024-01697-w>.

Supplementary information The online version contains supplementary material available at <https://doi.org/10.1038/s41477-024-01697-w>.

Correspondence and requests for materials should be addressed to Ji-Long Liu.

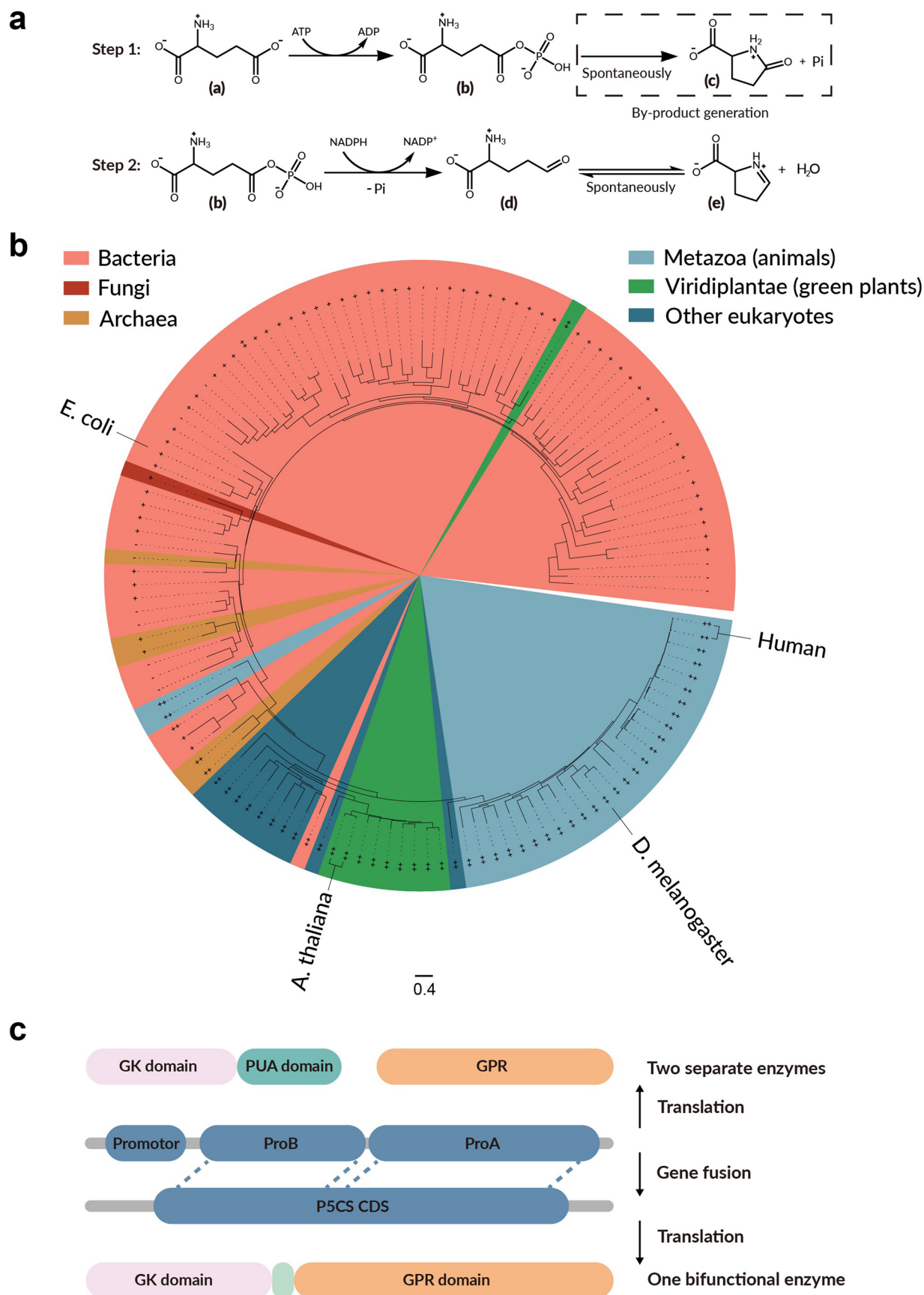
Peer review information *Nature Plants* thanks Alisdair Fernie, Arnould Savouré and László Szabados for their contribution to the peer review of this work.

Reprints and permissions information is available at www.nature.com/reprints.

Publisher's note Springer Nature remains neutral with regard to jurisdictional claims in published maps and institutional affiliations.

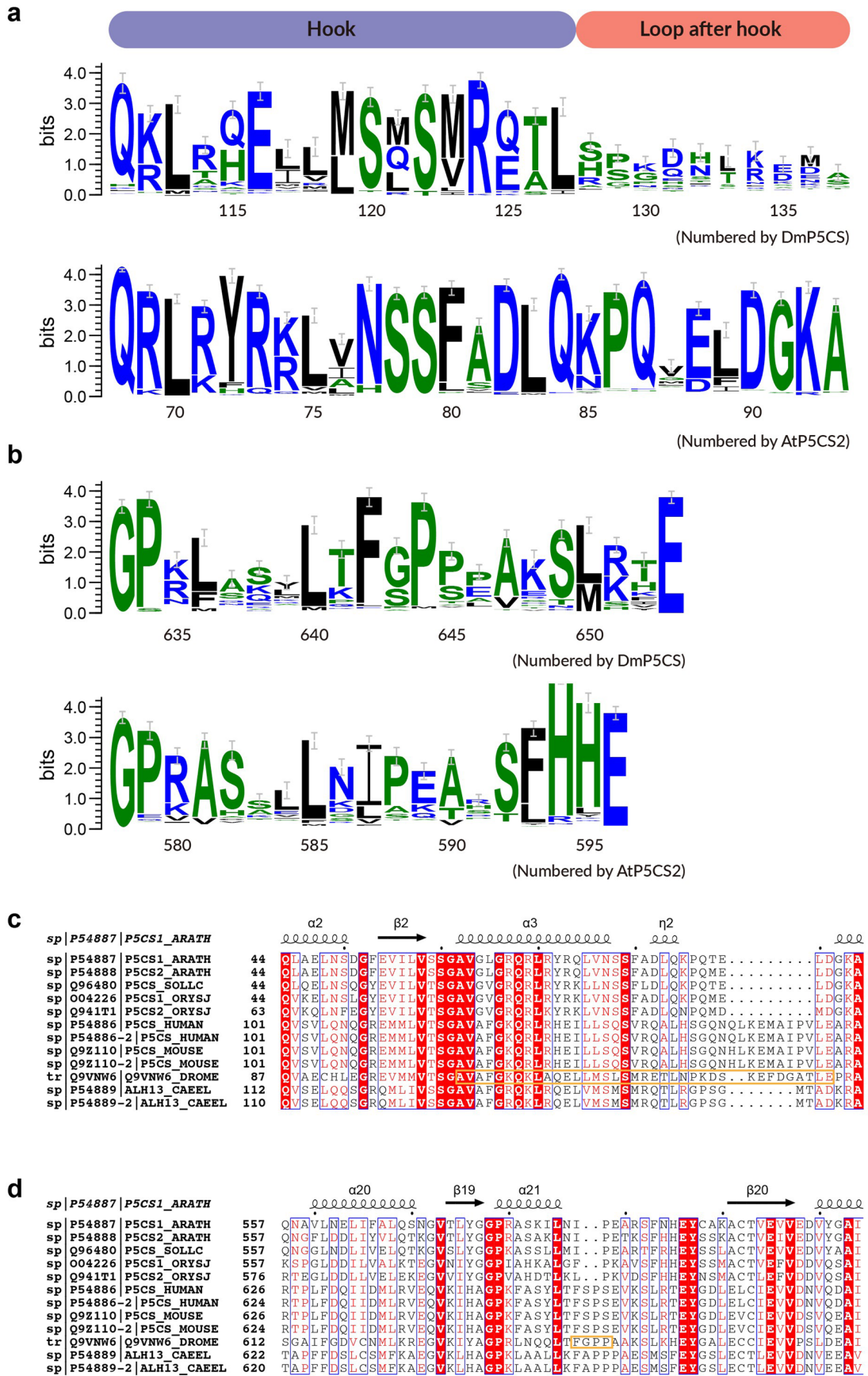
Open Access This article is licensed under a Creative Commons Attribution 4.0 International License, which permits use, sharing, adaptation, distribution and reproduction in any medium or format, as long as you give appropriate credit to the original author(s) and the source, provide a link to the Creative Commons licence, and indicate if changes were made. The images or other third party material in this article are included in the article's Creative Commons licence, unless indicated otherwise in a credit line to the material. If material is not included in the article's Creative Commons licence and your intended use is not permitted by statutory regulation or exceeds the permitted use, you will need to obtain permission directly from the copyright holder. To view a copy of this licence, visit <http://creativecommons.org/licenses/by/4.0/>.

© The Author(s) 2024



Extended Data Fig. 1 | Function and evolution of GK and GPR. (a) Two-step reaction catalyzed by GK and GPR. A possible side reaction is shown in the dashed box. a: L-glutamate. b: G5P. c: GSA. d: L-Pyrroline-5-carboxylate. e: Delta-1-pyrroline-5-carboxylate. (b) Phylogenetic tree of GK and P5CS proteins. Domain organization

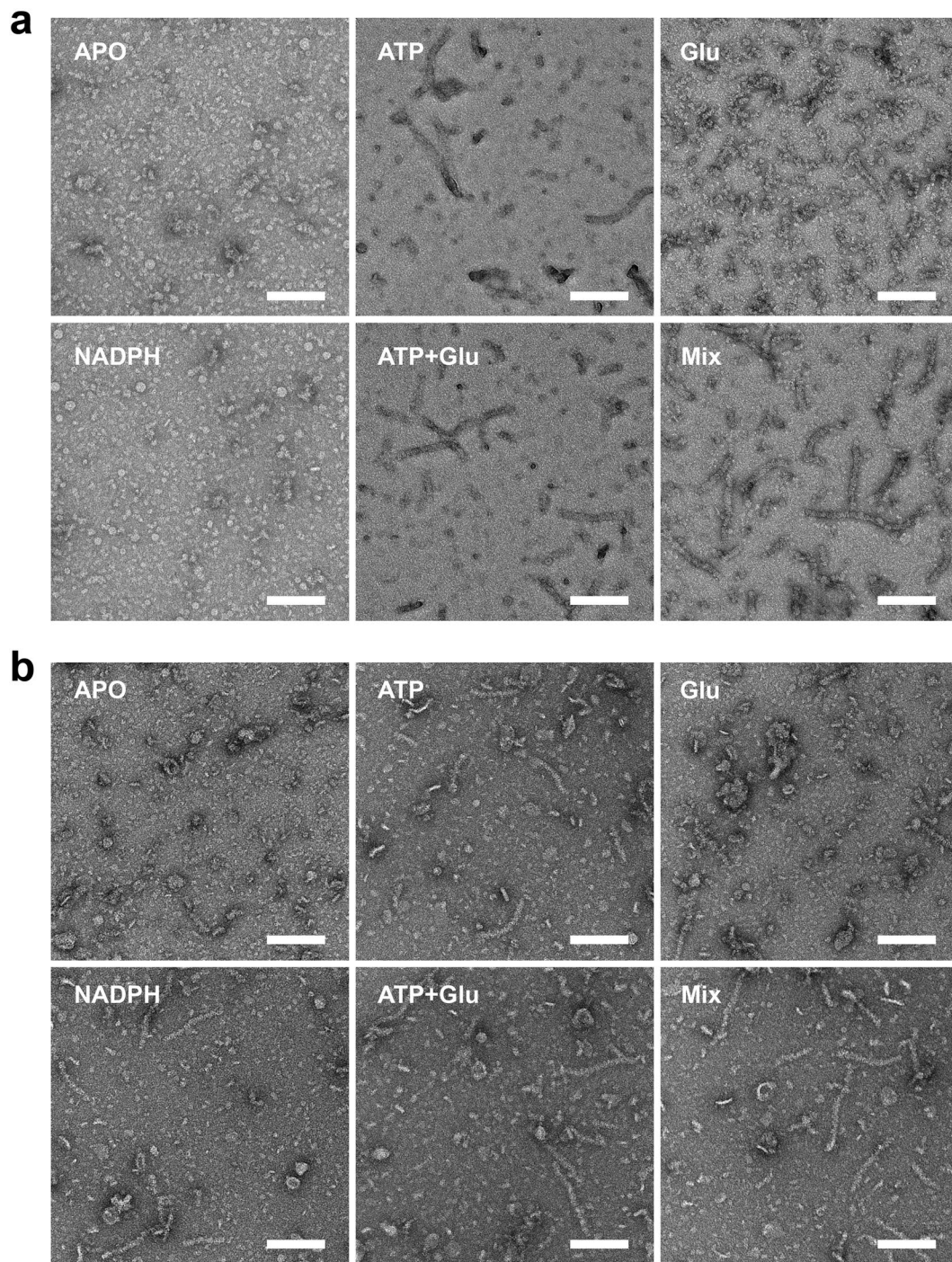
of these GK and P5CS is represented with marker at the extension of each clade, where '-' represent GK without PUA domain, '+' represent GK with PUA domain, and '++' represent P5CS. (c) Scheme of the fusion of GK and GPR during evolution.



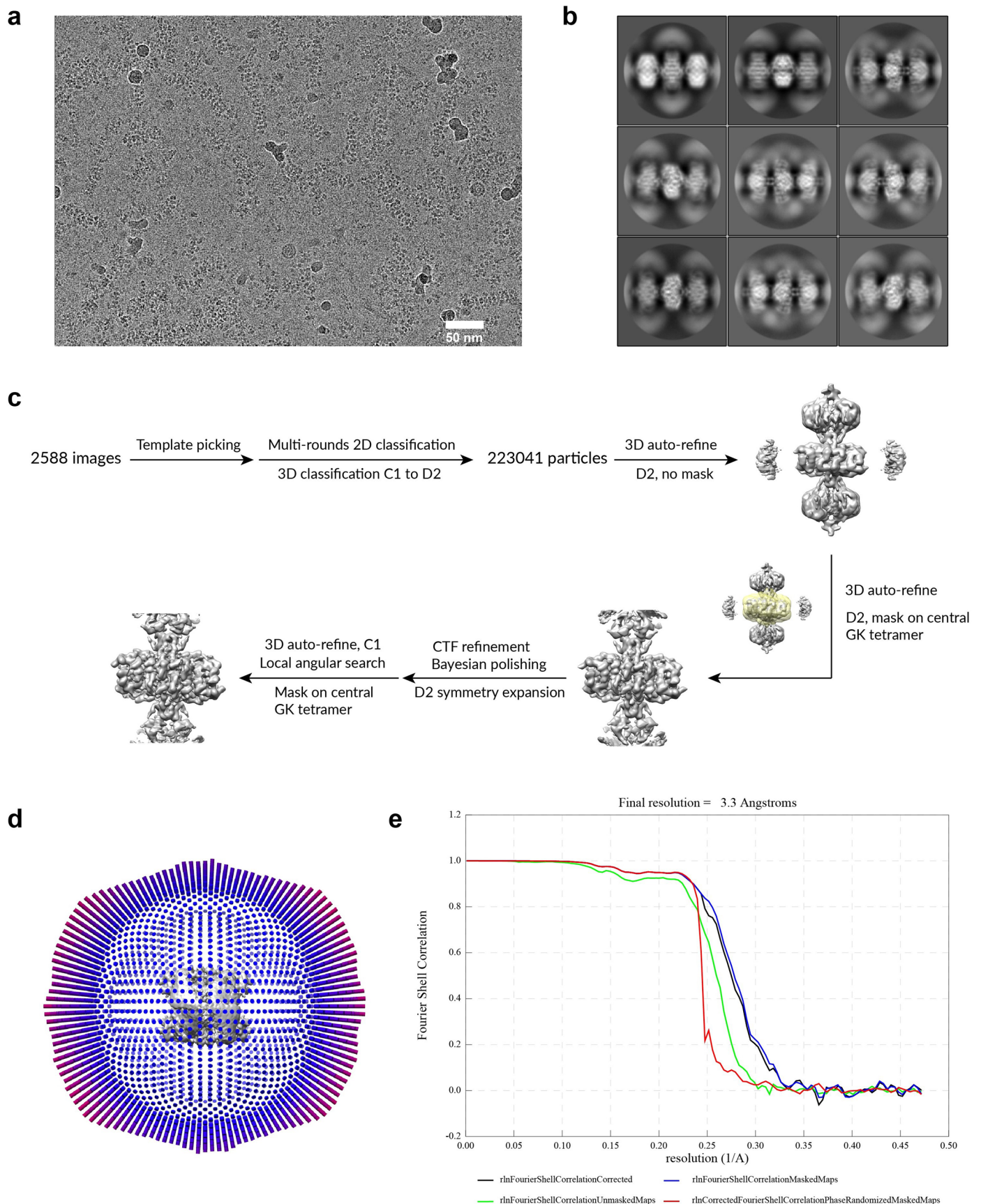
Extended Data Fig. 2 | See next page for caption.

Extended Data Fig. 2 | Alignment results of some representative P5CS sequences. Part of sequence logo of aligned P5CS around (a) hook and (b) contact loop. The reference residue number at the bottom is numbered based on DmP5CS and AtP5CS2. (c) Sequence alignment result around hook motif. Residues corresponding to hook and following loop of DmP5CS are labeled with orange box. (d) Sequence alignment result around contact loop. Residues

corresponding to the conserved motif 'FXPX' in DmP5CS are labeled with orange box. Sequences used for (c) and (d) were (from top to bottom): *A. thaliana* P5CS1, *A. thaliana* P5CS2, tomato P5CS, rice P5CS1, rice P5CS2, human P5CS, human P5CS (isoform), mouse P5CS, mouse P5CS (isoform), *D. melanogaster* P5CS, *C. elegans* P5CS, *C. elegans* P5CS (isoform).

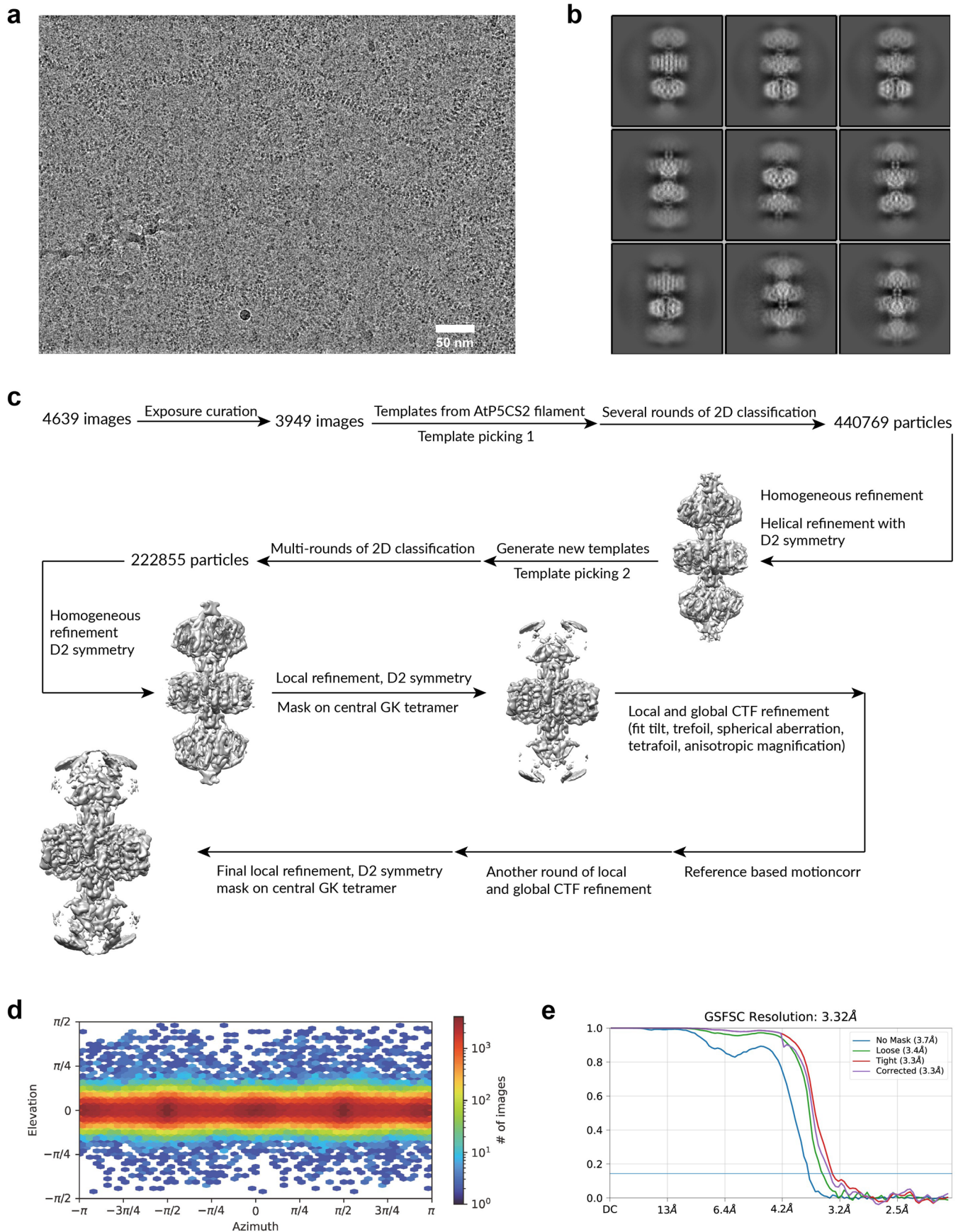


Extended Data Fig. 3 | Representative negative staining images of AtP5CS. Negative staining images of (a) AtP5CS2 and (b) AtP5CS1 incubated with different substrates. Scale bar: 150 nm. The negative staining experiments have been repeated for 3 times with similar results and each time more than ten different areas were checked.

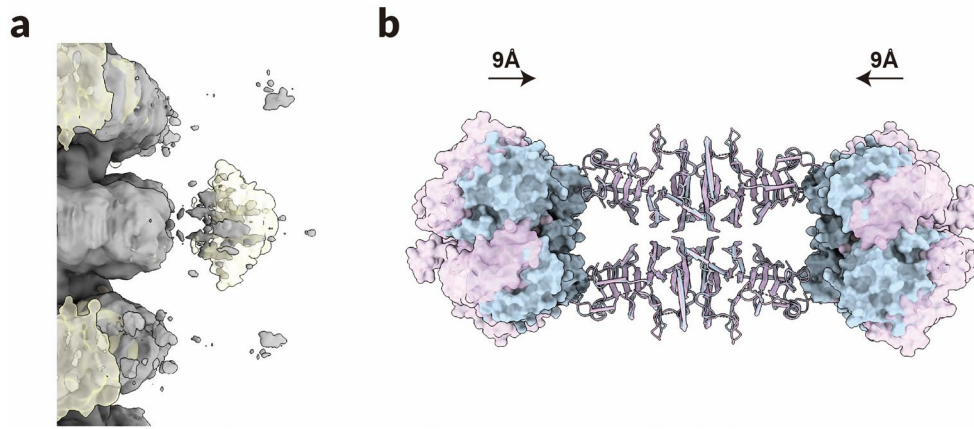


Extended Data Fig. 4 | Data processing of AtP5CS2. (a) Representative micrograph (from 2588 micrographs) after motion correction. **(b)** Representative 2D classification results. **(c)** Workflow for reconstruction

AtP5CS2 filament and focus refinement of GK tetramer. **(d)** Angular distribution (top view) of final GK tetramer reconstruction. Particles had been D2 expanded. **(e)** FSC curves for focus refined GK tetramer.

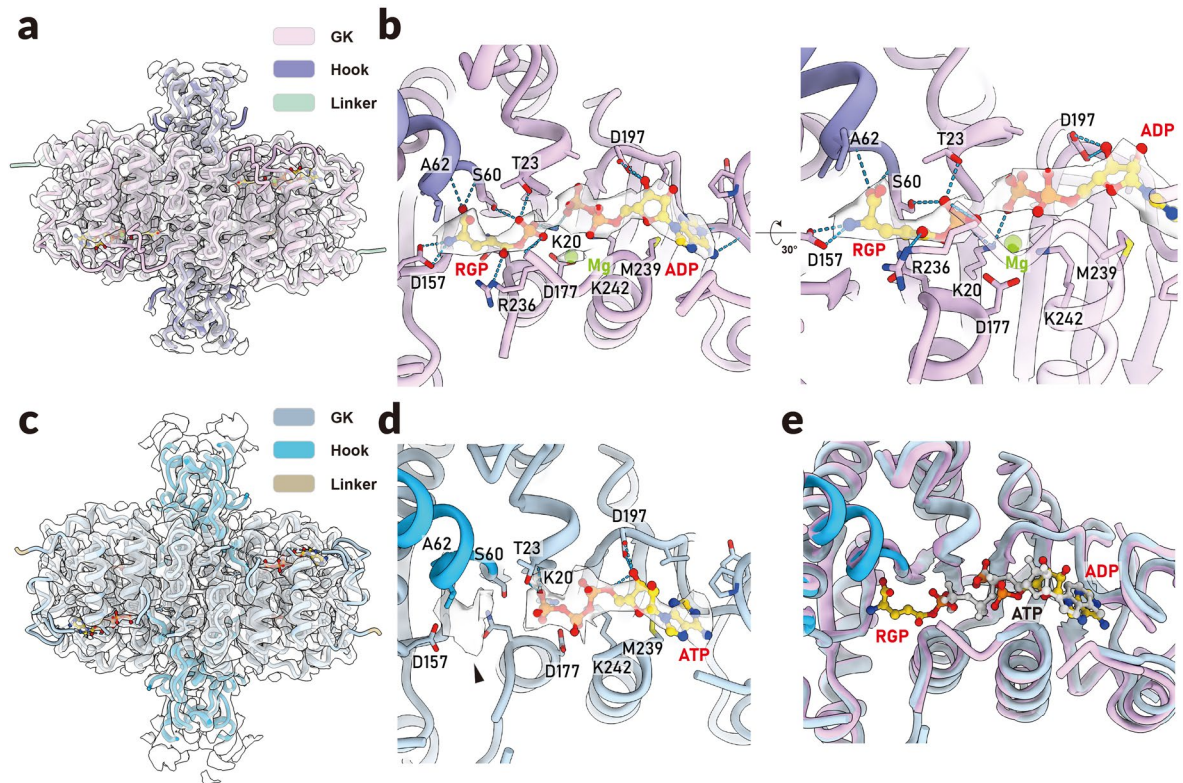


Extended Data Fig. 5 | Data processing of AtP5CS1. (a) Representative micrograph (from 4639 micrographs) after motion correction. **(b)** Representative 2D classification results. **(c)** Workflow for reconstruction AtP5CS1 filament and focus refinement of GK tetramer. **(d)** Angular distribution of focus refined GK tetramer reconstruction. **(e)** FSC curves for focus refined GK tetramer.



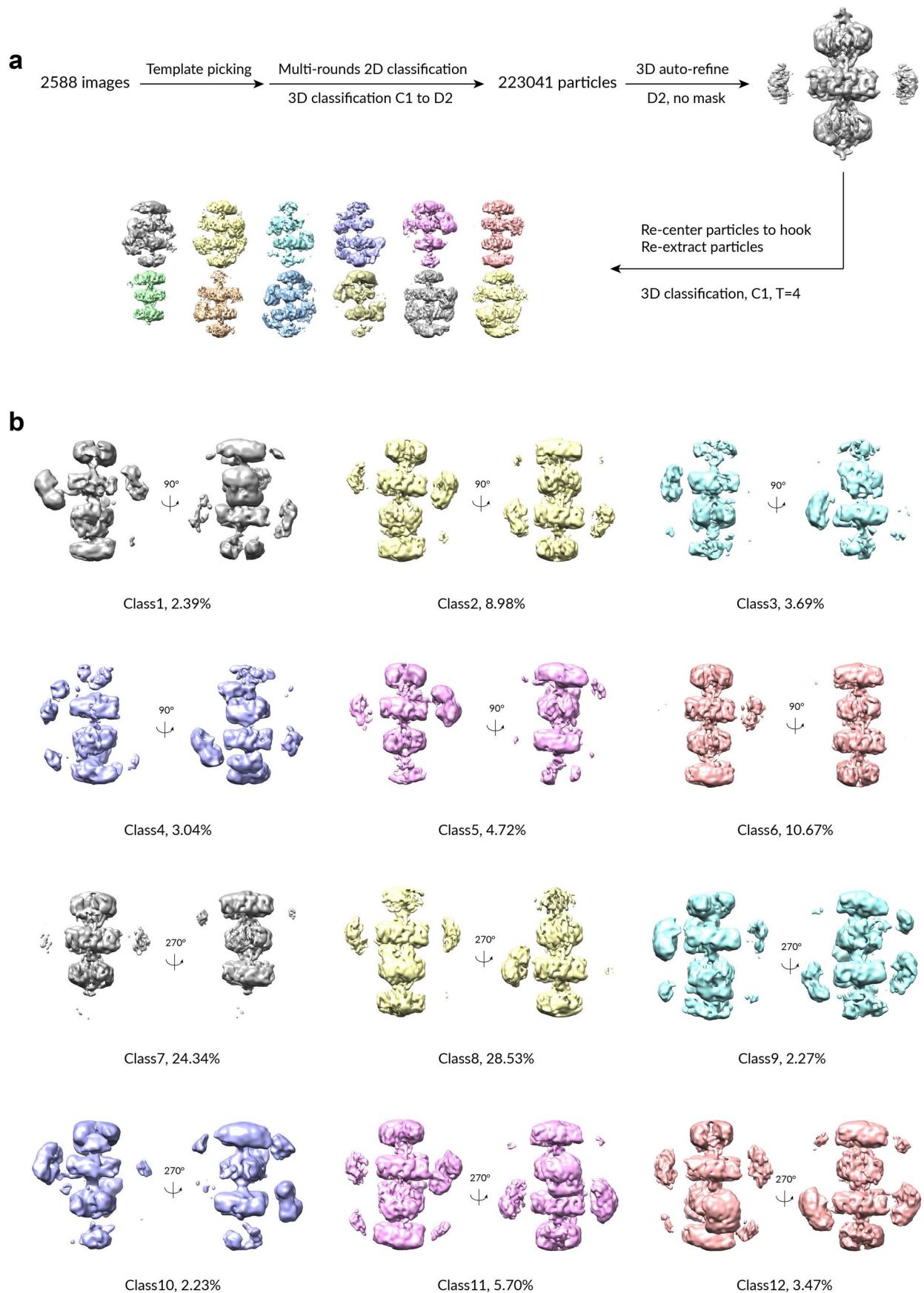
Extended Data Fig. 6 | The comparison of map and model between AtP5CS1 and AtP5CS2. (a) Map at low contour level of AtP5CS1 and AtP5CS2. Maps of AtP5CS1 and AtP5CS2 are displayed by grey and transparent yellow respectively.

(b) Models of AtP5CS1 and AtP5CS2 are aligned by GK tetramer and colored by blue and pink respectively. The shift of GPR along the symmetry axis is measured and indicated by the black arrow.

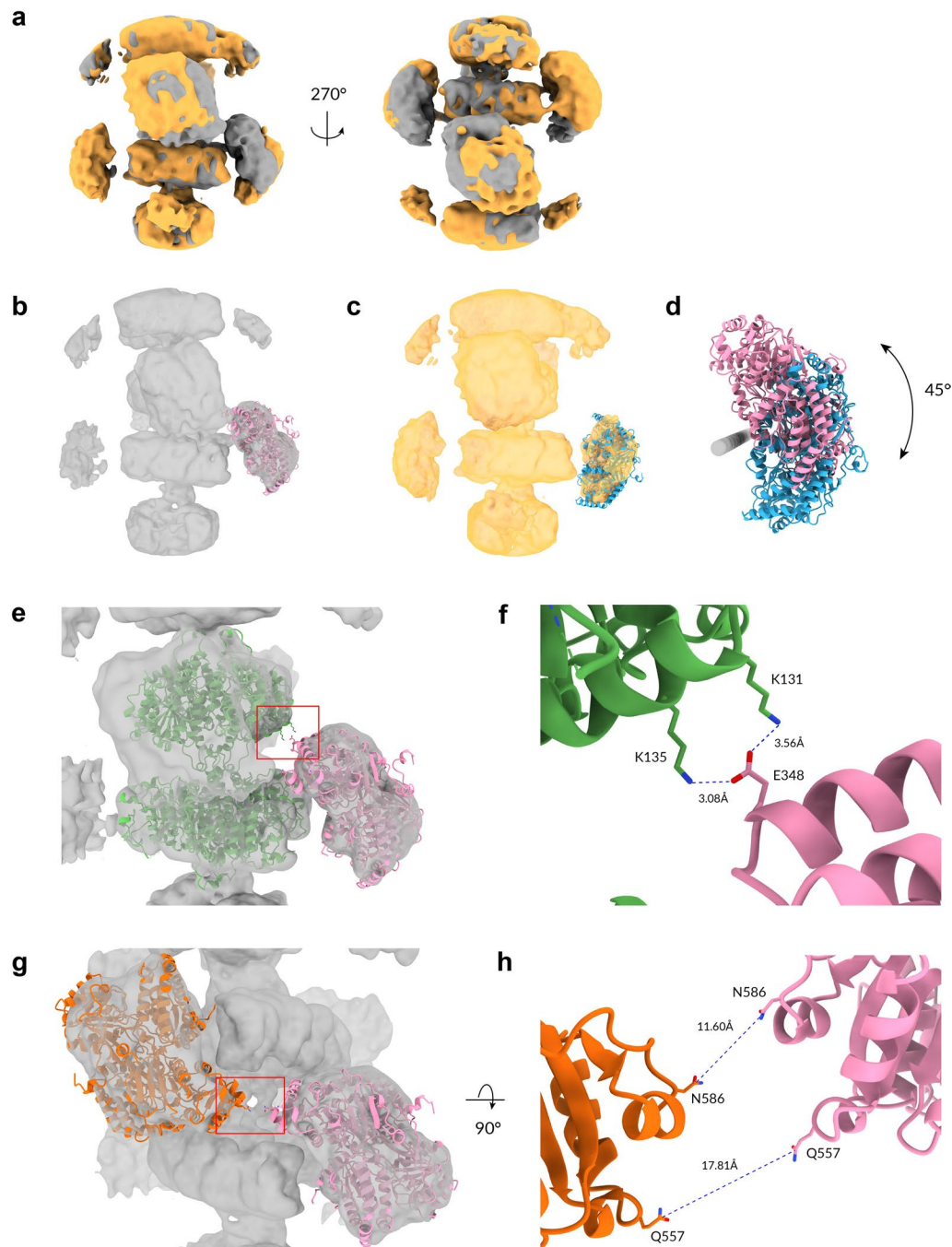


Extended Data Fig. 7 | Ligands binding of AtP5CS GK domain. (a) Map and model of AtP5CS2 GK domain. The map generated by focus-refinement is presented by a transparent surface. The 'hook' region of GK domain is colored by purple. (b) The ligand binding pocket of AtP5CS2 GK domain. RGP and ADP, the products of GK domain are colored by gold. And their densities are displayed by the white transparent surface. Surrounding amino acids and potential

interactions are indicated. (c) Map and model of AtP5CS1 GK domain. The map generated by focus-refinement is presented by a transparent surface. The 'hook' region of GK domain is colored by blue. (d) The ligand binding pocket of AtP5CS1 GK domain. ATP, the substrate of GK domain is colored by gold. Potential density of the substrate glutamate is also displayed, marked with black pin. (e) The comparison of GK pockets between AtP5CS1 and AtP5CS2.

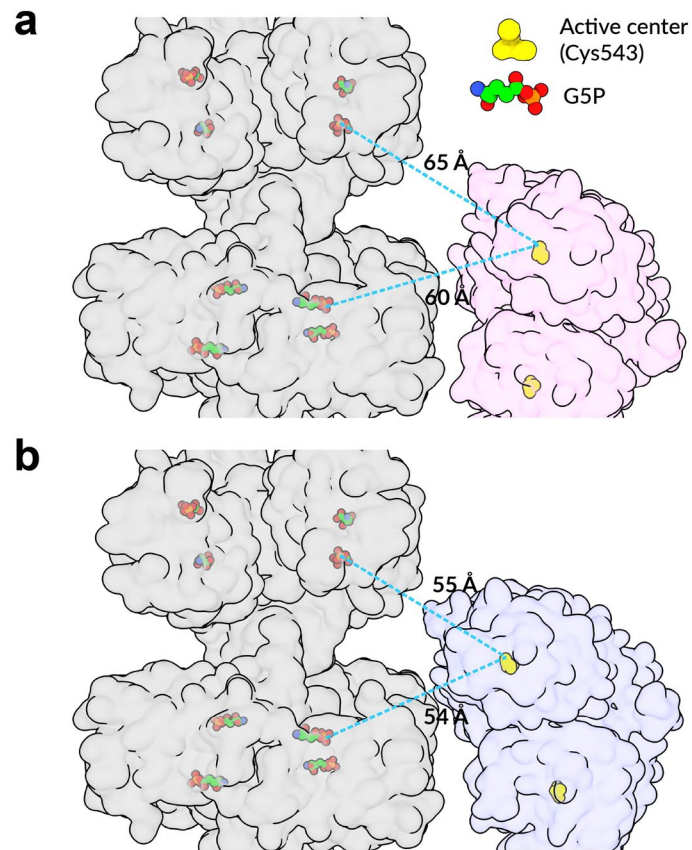


Extended Data Fig. 8 | 3D classification to visualize GPR of AtP5CS2. (a) Workflow for GPR 3D classification. After the first reconstruction for AtP5CS2, particles were re-centered to hook and re-extracted. **(b)** Display of 12 classes. GPR can be visualized in most classes with highly dynamic positions.



Extended Data Fig. 9 | Dynamic positions of GPR dimers. (a) Superposition of class11 (gray) and class12 (orange) maps. GPR dimers show different locations in these two classes. (b) AlphaFold2 model for GPR dimer is fitted into class 11 map. (c) AlphaFold2 model for GPR dimer is fitted into class 12 map. (d) Relative rotation between GPR dimers in class 11 (pink) and class 12 (blue). The gray bar represents the rotation axis. (e) One GPR dimer model (AlphaFold2, pink) and two GK tetramer models (green) are fitted into class 11 map. The potential

interaction region is label with red box. (f) Zoom in view of the red box in panel E. Rotamers of these displayed residues are manually adjusted in UCSF Chimera with Dunbrack 2010 library. (g) Two GPR dimer models (AlphaFold2) are fitted into class 11 map. The potential interaction region is label with red box. (h) Zoom in view of the red box in panel G (rotated by 90°). Rotamers of these displayed residues are manually adjusted in UCSF Chimera with Dunbrack 2010 library.



Extended Data Fig. 10 | Comparison of distances between the catalytic centers of GK and GPR during the motion of AtP5CS filament. (a) GPR dimer locates at the 'central position' (AlphaFold model fitted in consensus map). The distance between catalytic centers of GK and GPR is represented by the distance

of G5P and the catalytic residue C543. **(b)** GPR dimer rotates to the farthest position (AlphaFold model fitted in class I1 map). Distance measurement is the same as panel a.

Reporting Summary

Nature Portfolio wishes to improve the reproducibility of the work that we publish. This form provides structure for consistency and transparency in reporting. For further information on Nature Portfolio policies, see our [Editorial Policies](#) and the [Editorial Policy Checklist](#).

Statistics

For all statistical analyses, confirm that the following items are present in the figure legend, table legend, main text, or Methods section.

- | n/a | Confirmed |
|-------------------------------------|--|
| <input type="checkbox"/> | <input checked="" type="checkbox"/> The exact sample size (n) for each experimental group/condition, given as a discrete number and unit of measurement |
| <input type="checkbox"/> | <input checked="" type="checkbox"/> A statement on whether measurements were taken from distinct samples or whether the same sample was measured repeatedly |
| <input type="checkbox"/> | <input checked="" type="checkbox"/> The statistical test(s) used AND whether they are one- or two-sided <i>Only common tests should be described solely by name; describe more complex techniques in the Methods section.</i> |
| <input checked="" type="checkbox"/> | <input type="checkbox"/> A description of all covariates tested |
| <input checked="" type="checkbox"/> | <input type="checkbox"/> A description of any assumptions or corrections, such as tests of normality and adjustment for multiple comparisons |
| <input type="checkbox"/> | <input checked="" type="checkbox"/> A full description of the statistical parameters including central tendency (e.g. means) or other basic estimates (e.g. regression coefficient) AND variation (e.g. standard deviation) or associated estimates of uncertainty (e.g. confidence intervals) |
| <input type="checkbox"/> | <input checked="" type="checkbox"/> For null hypothesis testing, the test statistic (e.g. F , t , r) with confidence intervals, effect sizes, degrees of freedom and P value noted <i>Give P values as exact values whenever suitable.</i> |
| <input checked="" type="checkbox"/> | <input type="checkbox"/> For Bayesian analysis, information on the choice of priors and Markov chain Monte Carlo settings |
| <input checked="" type="checkbox"/> | <input type="checkbox"/> For hierarchical and complex designs, identification of the appropriate level for tests and full reporting of outcomes |
| <input checked="" type="checkbox"/> | <input type="checkbox"/> Estimates of effect sizes (e.g. Cohen's d , Pearson's r), indicating how they were calculated |

Our web collection on [statistics for biologists](#) contains articles on many of the points above.

Software and code

Policy information about [availability of computer code](#)

Data collection Unicorn (Cytiva, v7.7), SerialEM (v3), SoftMax Pro (v6.3)

Data analysis RELION (v3.3), MotionCor2 (v1.4.5), CTFFIND4 (v4.1.10), UCSF Chimera (v1.15), UCSF ChimeraX (v1.4), AlphaFold2 (DeepMind, v2.3), Coot (v0.9.8), FigTree (v1.4.4), Phenix (v1.20.1), ImageJ (1.53), MAFFT (v7.511), MS Excel (v16.0), GraphPad Prism (v9), trimAl (1.2rev59), IQTREE (v2.2), WebLogo (v3), Esript (v3)

For manuscripts utilizing custom algorithms or software that are central to the research but not yet described in published literature, software must be made available to editors and reviewers. We strongly encourage code deposition in a community repository (e.g. GitHub). See the Nature Portfolio [guidelines for submitting code & software](#) for further information.

Data

Policy information about [availability of data](#)

All manuscripts must include a [data availability statement](#). This statement should provide the following information, where applicable:

- Accession codes, unique identifiers, or web links for publicly available datasets
- A description of any restrictions on data availability
- For clinical datasets or third party data, please ensure that the statement adheres to our [policy](#)

The cryo-EM map generated for this manuscript is available from the EMDB (<https://www.ebi.ac.uk/emdb/>) with accession code EMD-35901 and EMD-38855. The

protein model generated for this manuscript is available from RCSB PDB (<https://www.rcsb.org/>) with accession code PDB-8J0F and PDB-8Y2H. In this study following data were used: DmP5CS filament structures (PDB: 7WX3, 7WXI).

Research involving human participants, their data, or biological material

Policy information about studies with [human participants or human data](#). See also policy information about [sex, gender \(identity/presentation\), and sexual orientation](#) and [race, ethnicity and racism](#).

Reporting on sex and gender

Reporting on race, ethnicity, or other socially relevant groupings

Population characteristics

Recruitment

Ethics oversight

Note that full information on the approval of the study protocol must also be provided in the manuscript.

Field-specific reporting

Please select the one below that is the best fit for your research. If you are not sure, read the appropriate sections before making your selection.

Life sciences Behavioural & social sciences Ecological, evolutionary & environmental sciences

For a reference copy of the document with all sections, see [nature.com/documents/nr-reporting-summary-flat.pdf](https://www.nature.com/documents/nr-reporting-summary-flat.pdf)

Life sciences study design

All studies must disclose on these points even when the disclosure is negative.

| | |
|-----------------|--|
| Sample size | Statistical methods were not employed to predefine sample sizes. Instead, the data size for cryo-EM was dictated by the microscope's availability and the particle density on the grids. Meanwhile, the sample sizes for functional assays and negative staining microscopy were determined by the reproducibility of recordings, typically set at 3. This n=3 parallelism adheres to the fundamental biological principle of parallelism. |
| Data exclusions | During cryo-EM data processing, particle images of damaged, incomplete, or contaminated structures were filtered out by both 2D and 3D classification procedures. |
| Replication | WT and mutant AtP5CS1 and AtP5CS2 protein were successfully purified for three times. Negative staining for each conduction was replicated for more than three times. To measure the length of P5CS filament, about 10 photographs were taken from different holes in a same EM grid, and these photographs were combined together for measurement. For enzyme activity, three successful technical replications were applied. |
| Randomization | For structure determination, all particles were randomly split into two groups, one for refinement and the other for validation. For the negative electron microscopy, micrographs were captured randomly. |
| Blinding | The investigators were not blinded to the group allocation, because no grouping was needed for this study. |

Reporting for specific materials, systems and methods

We require information from authors about some types of materials, experimental systems and methods used in many studies. Here, indicate whether each material, system or method listed is relevant to your study. If you are not sure if a list item applies to your research, read the appropriate section before selecting a response.

Materials & experimental systems

| n/a | Included in the study |
|-------------------------------------|--|
| <input checked="" type="checkbox"/> | <input type="checkbox"/> Antibodies |
| <input checked="" type="checkbox"/> | <input type="checkbox"/> Eukaryotic cell lines |
| <input checked="" type="checkbox"/> | <input type="checkbox"/> Palaeontology and archaeology |
| <input checked="" type="checkbox"/> | <input type="checkbox"/> Animals and other organisms |
| <input checked="" type="checkbox"/> | <input type="checkbox"/> Clinical data |
| <input checked="" type="checkbox"/> | <input type="checkbox"/> Dual use research of concern |
| <input checked="" type="checkbox"/> | <input type="checkbox"/> Plants |

Methods

| n/a | Included in the study |
|-------------------------------------|---|
| <input checked="" type="checkbox"/> | <input type="checkbox"/> ChIP-seq |
| <input checked="" type="checkbox"/> | <input type="checkbox"/> Flow cytometry |
| <input checked="" type="checkbox"/> | <input type="checkbox"/> MRI-based neuroimaging |